


Article

Ni Doped Co-MOF-74 Synergized with 2D $\text{Ti}_3\text{C}_2\text{T}_x$ MXene as an Efficient Electrocatalyst for Overall Water-Splitting

Ke Yu, Jingyuan Zhang, Yuting Hu, Lanqi Wang, Xiaofeng Zhang and Bin Zhao * 

School of Materials & Chemistry, University of Shanghai for Science and Technology, Shanghai 200093, China; 212203110@st.usst.edu.cn (K.Y.); 211590182@st.usst.edu.cn (J.Z.); 213353262@st.usst.edu.cn (X.Z.)

* Correspondence: zhaobin@usst.edu.cn

Abstract: Metal-organic framework (MOF)-based materials with abundant pore structure, large specific surface area, and atomically dispersed metal centers are considered as potential electrocatalysts for oxygen-evolution reaction (OER), while their ligand-saturated metal nodes are inert to electrocatalysis. In this work, heteroatom doping and interface engineering are proposed to improve the OER performance of Co-MOF-74. Using two-dimensional $\text{Ti}_3\text{C}_2\text{T}_x$ MXene as a conductive support, Ni-doped Co-MOF-74 (CoNi-MOF-74/MXene/NF) was in situ synthesized through a hydrothermal process, which exhibits excellent OER and hydrogen evolution reaction (HER) properties. For OER, the CoNi-MOF-74/MXene/NF achieves a current density of $100 \text{ mA}/\text{cm}^2$ at an overpotential of only 256 mV, and a Tafel slope of 40.21 mV/dec. When used for HER catalysis, the current density of $10 \text{ mA}/\text{cm}^2$ is reached at only 102 mV for the CoNi-MOF-74/MXene/NF. In addition, the two-electrode electrolyzer with CoNi-MOF-74/MXene/NF as both the cathode and anode only requires 1.49 V to reach the current density of $10 \text{ mA}/\text{cm}^2$. This work provides a new approach for the development of bimetallic MOF-based electrocatalysts.

Keywords: Ni doping; MOF-74; MXene; overall water-splitting



Citation: Yu, K.; Zhang, J.; Hu, Y.; Wang, L.; Zhang, X.; Zhao, B. Ni Doped Co-MOF-74 Synergized with 2D $\text{Ti}_3\text{C}_2\text{T}_x$ MXene as an Efficient Electrocatalyst for Overall Water-Splitting. *Catalysts* **2024**, *14*, 184. <https://doi.org/10.3390/catal14030184>

Academic Editor: Edward G. Gillan

Received: 4 February 2024

Revised: 4 March 2024

Accepted: 5 March 2024

Published: 7 March 2024



Copyright: © 2024 by the authors. Licensee MDPI, Basel, Switzerland. This article is an open access article distributed under the terms and conditions of the Creative Commons Attribution (CC BY) license (<https://creativecommons.org/licenses/by/4.0/>).

1. Introduction

Electrocatalytic water splitting offers an appealing, rapid, and sustainable pathway for producing hydrogen in a clean manner, reducing reliance on conventional fossil fuels and contributing to a healthier environment [1–3]. However, both half reactions in the water splitting process, the hydrogen evolution reaction (HER) and oxygen evolution reaction (OER), suffer from sluggish reaction kinetics due to their multi-step proton coupled electron transfer processes [4]. Precious metal catalysts, such as Pt/C and IrO_2 , are highly coveted for their ability to function as electrocatalysts for both HER and OER. These catalysts exhibit ultralow overpotential and exceptional long-term durability, making them ideal for industrial purposes. Unfortunately, the rarity and high cost of these materials render electrocatalytic water splitting a costly process [1,5]. Therefore, there is a crucial need to develop affordable and durable electrocatalysts based on non-noble metals [6].

Recently, metal-organic frameworks (MOFs) have become known for their high porosity, large surface area, customizable composition, abundant active sites, and well-ordered nanostructures that facilitate effective ionic and electron transfer [7]. MOFs are structures that consist of organic ligands and metal ions or clusters coordinated together [8]. Because there are multiple metal ions and organic ligands with unique properties, they can coordinate with each other to form a wide range of MOFs [9]. For MOFs, it is not only suitable for alkaline environments but also a perfect platform for designing efficient and cost-effective acidic OER catalysts in acidic environments. For example, Xu et al. [10] provide a comprehensive review of recent advances in MOF-based acidic OER catalysts and discuss some catalyst design strategies aimed at improving the acidic OER catalytic performance of MOF-based candidate catalysts. Among them, MOF-74 stands out with a porous channel,

featuring a unique one-dimensional hexagonal shape. First synthesized by Yaghi's team in 2005, MOF-74 has the general formula $M_2(\text{DOBDC})$ (M: Co, Ni, Zn, Mg, Mn, Fe, H_4DOBDC : 2,5-dihydroxyterephthalic acid) [11]. In the MOF-74 crystal structure, each metal ion is coordinated to five oxygen atoms, with an associated unsaturated coordination site [12]. These properties have made it renowned for the divalent tunability of its metal nodes, which offers unlimited possibilities for electrocatalyst design in terms of topology, pore size and functionality [13]. Among the various MOF-based OER catalysts, the Co-based MOFs have received a great deal of attention due to their high activity and stability [14,15]. Theoretical calculations and experimental results indicate that incorporating one or more species can significantly improve electrocatalytic performance due to a synergistic effect. This includes improved charge transfer between dopants and host metal atoms and optimized electronic structures to reduce kinetic energy barriers during catalytic processes [16]. Unfortunately, most MOFs are natively suffering from poor electrical conductivity [17]. Therefore, the combination of MOFs and conductive nanostructures is expected to further enhance the performance in various electrocatalytic processes [8].

MXenes, an emerging group of 2D materials, are prepared through selective removal of the A layers from MAX phases (M is an early transition metal, A is an A group element, and X is either C and/or N) [18]. They display excellent electrical conductivity, surface hydrophilicity, and stability. Additionally, MXenes, with low work function and electronegative surfaces, serve as promising substrates to modify the electrophilicity of active sites in catalysts, thereby regulating catalytic properties in multicomponent catalyst systems [8].

Herein, composite electrocatalysts with self-supported Ni-doped Co-MOF-74 on $\text{Ti}_3\text{C}_2\text{T}_x$ MXene (designated as CoNi-MOF-74/MXene/NF) were synthesized through a facile method consisting of electrostatic deposition and hydrothermal synthesis. This method provides a high degree of control over the synthesis process, resulting in efficient electrocatalysts. The incorporation of Ni modifies the electronic structure of Co sites in the MOF-74 and promotes the formation of high oxidation-state Co^{3+} , ultimately improving the OER performance [6]. Moreover, the robust interfacial interaction and electronic coupling between MOF and $\text{Ti}_3\text{C}_2\text{T}_x$ nanosheets facilitate fast charge transfer kinetics and provide a stable structure, both crucial factors in optimizing catalytic performance [19]. The $\text{CoNi}_{0.04}\text{-MOF-74/MXene/NF}$ composite exhibits superior catalytic activity for both HER and OER in alkaline electrolytes, outperforming individual Co-MOF-74 and MXene at current densities of $10 \text{ mA}\cdot\text{cm}^{-2}$ and $100 \text{ mA}\cdot\text{cm}^{-2}$, respectively. Specifically, the catalyst achieves a current density of $10 \text{ mA}\cdot\text{cm}^{-2}$ and $100 \text{ mA}\cdot\text{cm}^{-2}$ at overpotentials of 102 mV and 256 mV for HER and OER, respectively. When employed as both cathode and anode catalysts in the two-electrode electrolyzer, the $\text{CoNi}_{0.04}\text{-MOF-74/MXene/NF}$ heterostructure catalyst achieves a current density of $10 \text{ mA}\cdot\text{cm}^{-2}$ at 1.49 V in alkaline solution, surpassing the performance of a traditional Pt/C || IrO_2 couple. Remarkably, the electrolyzer maintains a nearly constant current density over 40 continuous hours, demonstrating its satisfactory long-term durability. These findings not only demonstrate the potential of $\text{CoNi}_{0.04}\text{-MOF-74/MXene/NF}$ for practical applications but also offer insights for the development of other efficient MOF-based composite catalysts.

2. Results and Discussion

2.1. Catalyst Synthesis and Characterization

Figure 1 schematically illustrates the synthetic process of CoNi-MOF-74/MXene/NF using the two-step method. Firstly, the $\text{Ti}_3\text{C}_2\text{T}_x$ MXene nanosheets prepared using the MILD method were electrostatically deposited on nickel foam (NF). Scanning electron microscopy (SEM) images show that $\text{Ti}_3\text{C}_2\text{T}_x$ MXene with fewer layers was successfully prepared (Figure S1, Supplementary Materials). Due to the strong electrostatic interaction between the negatively charged $\text{Ti}_3\text{C}_2\text{T}_x$ MXene nanosheets and the positively charged NF, $\text{Ti}_3\text{C}_2\text{T}_x$ MXene can easily adhere to the three-dimensional framework of NF, imparting the black color to the substrate. SEM images reveal the even distribution of $\text{Ti}_3\text{C}_2\text{T}_x$ MXene nanosheets on the NF skeleton (Figure 2a). After that, CoNi-MOF-74 was grown in

situ on MXene/NF through a hydrothermal process. Taking advantage of the distinctive terminal groups of -OH and -F, the CoNi-MOF-74 can be successfully anchored to the surface of MXene. SEM observation shows that the bimetallic MOF-74 have the same identical crystal structure as the single metal MOF-74. In comparison with Co-MOF-74 (Figure 2c), all Ni-doped bimetallic MOF-74 show consistent and regular nanorod morphology (Figures 2b and S2 (Supplementary Materials)). Interestingly, a Co/Ni molar ratio of 25:1 results in a thinner and longer nanorod morphology for CoNi_{0.04}-MOF-74/MXene/NF, compared to CoNi_{0.1}-MOF-74/MXene/NF and CoNi_{0.03}-MOF-74/MXene/NF. This may be attributed to the influence of Ni atoms, which may promote MOF crystal growth along specific lattice planes while limiting growth in other lattice planes [16]. Figure 2b illustrates that the prepared CoNi-MOF-74 microrods exhibit a hexagonal structure and a smooth surface, with an average diameter of approximately 10 μm . Elemental mapping reveals a uniform dispersion of Co, Ni, O, and C within the rod-like structure of CoNi-MOF-74 (Figure 2d–h). Furthermore, the Energy-Dispersive X-ray Spectroscopy (EDS) analysis on CoNi_{0.04}-MOF-74/MXene/NF confirms the presence of Ti element, indicating the successful integration of MOF with MXene (Figure S3, Supplementary Materials).

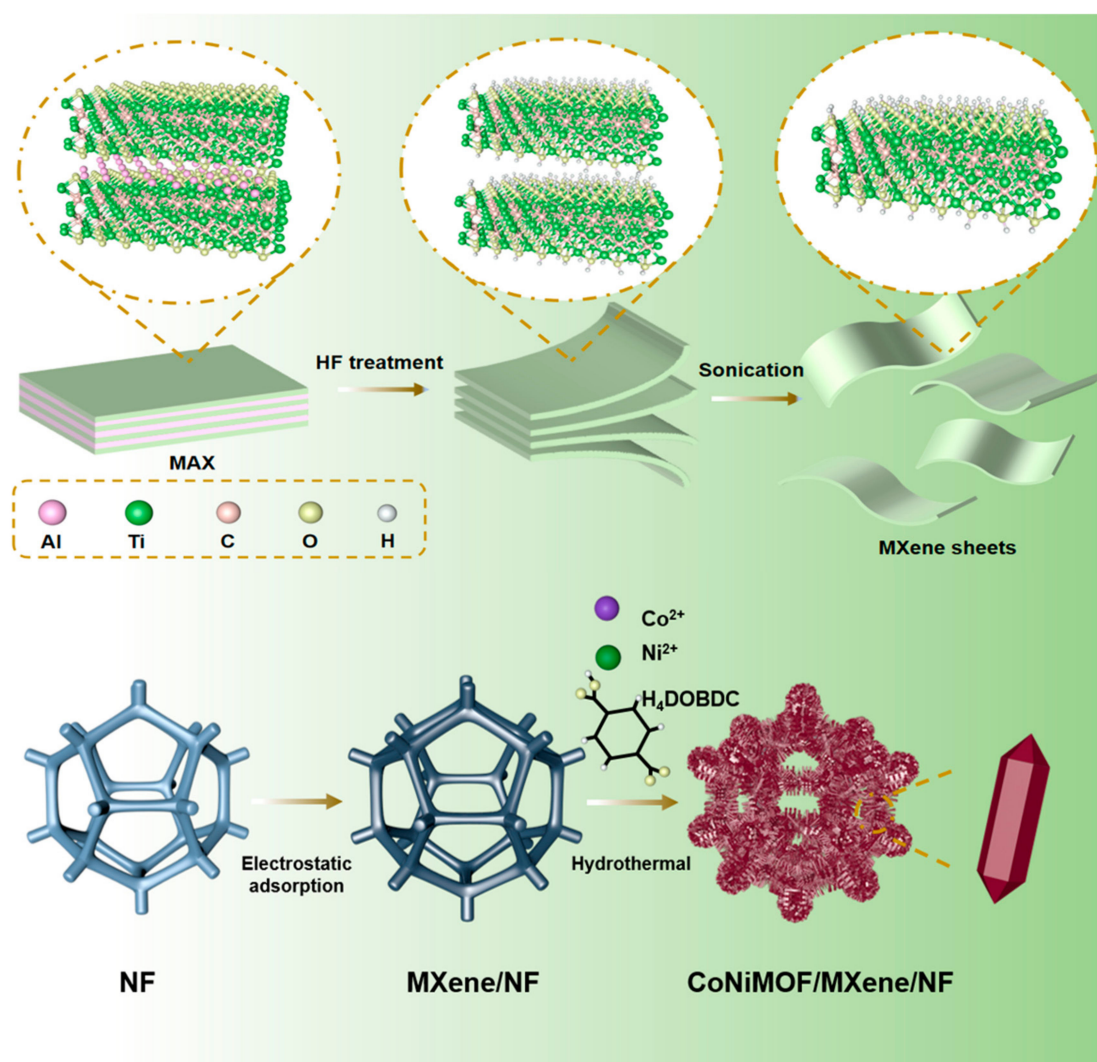


Figure 1. Schematic diagram of the preparation of CoNi-MOF-74/MXene/NF electrodes.

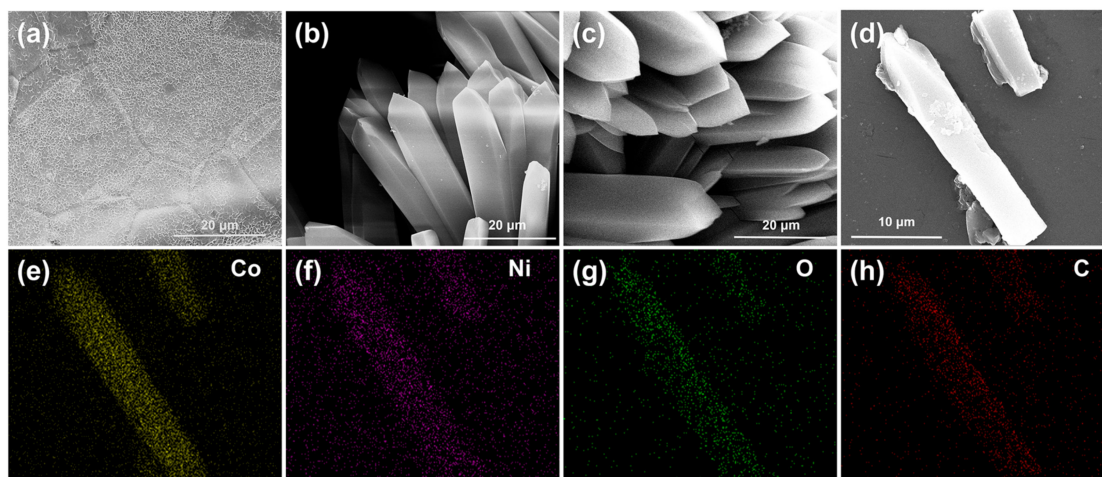


Figure 2. SEM images: (a) MXene/NF, (b) CoNi_{0.04}-MOF/MXene/NF, (c) Co-MOF-74/MXene/NF. SEM image (d) and corresponding elemental mappings of Co, Ni, O and C (e–h) of CoNi_{0.04}-MOF/MXene/NF.

X-ray diffraction (XRD) was used to characterize crystal structure of the as-synthesized catalysts. As shown in Figure S4 (Supplementary Materials), compared with the Ti₃AlC₂ phase, the (104) diffraction peak corresponding to the Al layer completely disappears after etching, confirming the successful preparation of MXene [20]. Figure 3a displays the XRD patterns of the prepared CoNi-MOF-74 samples, which match well with the simulated peaks of MOF-74. Upon closer examination (Figure 3a), the diffraction peaks associated with the bimetallic MOFs shift to a smaller angle, indicating the successful introduction of Ni element into the MOF-74 backbone, resulting in a larger interplanar crystal spacing [6,21,22]. Figure 3b presents the FT-IR spectra of the as-prepared MOF-74 and H₄DOBDC for comprehending the coordination between metal ions and H₄DOBDC. For Co-MOF-74 and bimetallic CoNi-MOF-74, the absorption peak observed above 800 cm⁻¹ corresponds to the organic ligand 2,5-dihydroxyterephthalic acid vibration. In the low wavenumber region, the peak at 585 cm⁻¹ indicates the M-O bond vibration, confirming the successful synthesis of CoNi-MOF-74 [7].

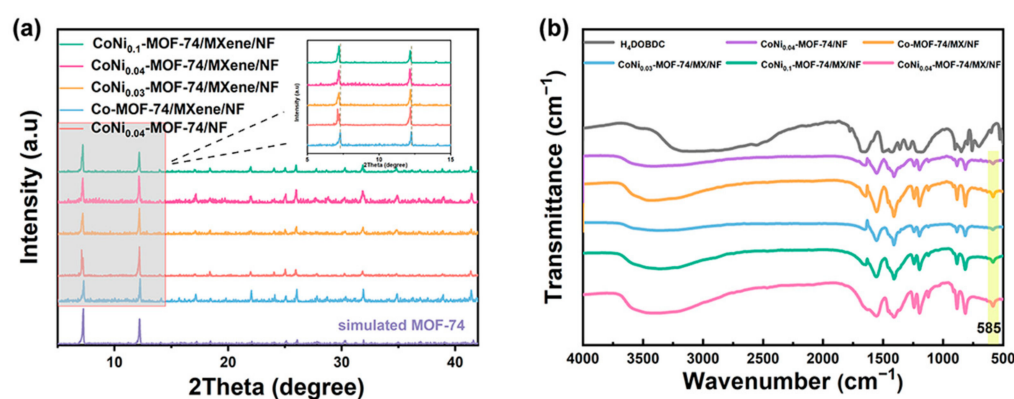


Figure 3. (a) XRD patterns, (b) FT-IR spectra of CoNi_{0.04}-MOF-74/MXene/NF, CoNi_{0.1}-MOF-74/MXene/NF, CoNi_{0.03}-MOF-74/MXene/NF, CoNi_{0.04}-MOF-74/NF and Co-MOF-74/MXene/NF.

Additionally, X-ray photoelectron spectroscopy (XPS) analysis was conducted to elucidate the chemical composition and states of CoNi_{0.04}-MOF-74/MXene. The general XPS survey spectra of CoNi_{0.04}-MOF-74/MXene, as depicted in Figure S5 (Supplementary Materials), confirm the presence of Co, Ni, Ti, C, and O elements. As illustrated in Figure 4a, the Co 2p high-resolution spectrum of CoNi_{0.04}-MOF-74/MXene reveals two peaks corresponding to Co 2p_{1/2} and Co 2p_{3/2}, providing evidence of the coexistence of Co²⁺ (797.8 and

782.2 eV) and Co^{3+} (796.4 and 780.6 eV) in $\text{CoNi}_{0.04}\text{-MOF-74/MXene}$ [23]. In comparison with Co-MOF-74/MXene , the atomic ratio of $\text{Co}^{3+}/\text{Co}^{2+}$ increases from 1.44 to 2.50 in $\text{CoNi}_{0.04}\text{-MOF-74/MXene}$ (Table S1, Supplementary Materials). Therefore, the incorporation of the Ni dopant can modify the electronic structure of Co species in Co-MOFs, resulting in a slightly higher oxidation state [24,25]. Since Co^{3+} is often considered as the main active site for OER, the increased content in this high oxidation state may be beneficial for enhancing OER catalytic activity [26–28]. Furthermore, the Ti 2p high-resolution spectrum (Figure 4b) shows peaks at 458.3 eV/464.5 eV and 455.7 eV/461.3 eV, attributed to Ti–O and Ti–C bonds, respectively [29]. The C1s spectrum (Figure 4c) suggests the possible presence of O=C–O (288.7 eV), C=O (288.1 eV), C–C (285.67 eV), C=C (284.48 eV), and C–Ti (282.5 eV) species [30,31]. And the deconvolution of the O 1s spectrum indicates the presence of absorbed water (533.0 eV), O=C–O (532.1 eV), C=O (531.3 eV), and M–O bond (530.3 eV) [8,32], as illustrated in Figure 4d. Noteworthy, compared with $\text{CoNi}_{0.04}\text{-MOF-74}$ directly grown on NF ($\text{CoNi}_{0.04}\text{-MOF-74/NF}$), both the Co 2p and Ni 2p peaks of $\text{CoNi}_{0.04}\text{-MOF-74/MXene/NF}$ exhibit a shift of 0.3–0.5 eV towards lower binding energies (Figure S6, Supplementary Materials). This shift underscores the significant electronic interactions at the interface of $\text{CoNi}_{0.04}\text{-MOF-74}$ and MXene, positively impacting the regulation of electrocatalytic activity. In the Raman spectrum of $\text{CoNi}_{0.04}\text{-MOF-74/MXene/NF}$ (Figure S7, Supplementary Materials), the stretching of the M–O (M=Co/Ni) bond was confirmed at 565.4 cm^{-1} , while the peak at 818.9 cm^{-1} is assigned to the C–H bending of the benzene ring [33]. Additionally, the peaks at 1274.8 and 1409.6 cm^{-1} correspond to C=O stretching and O–C–O symmetric stretching, respectively [34].

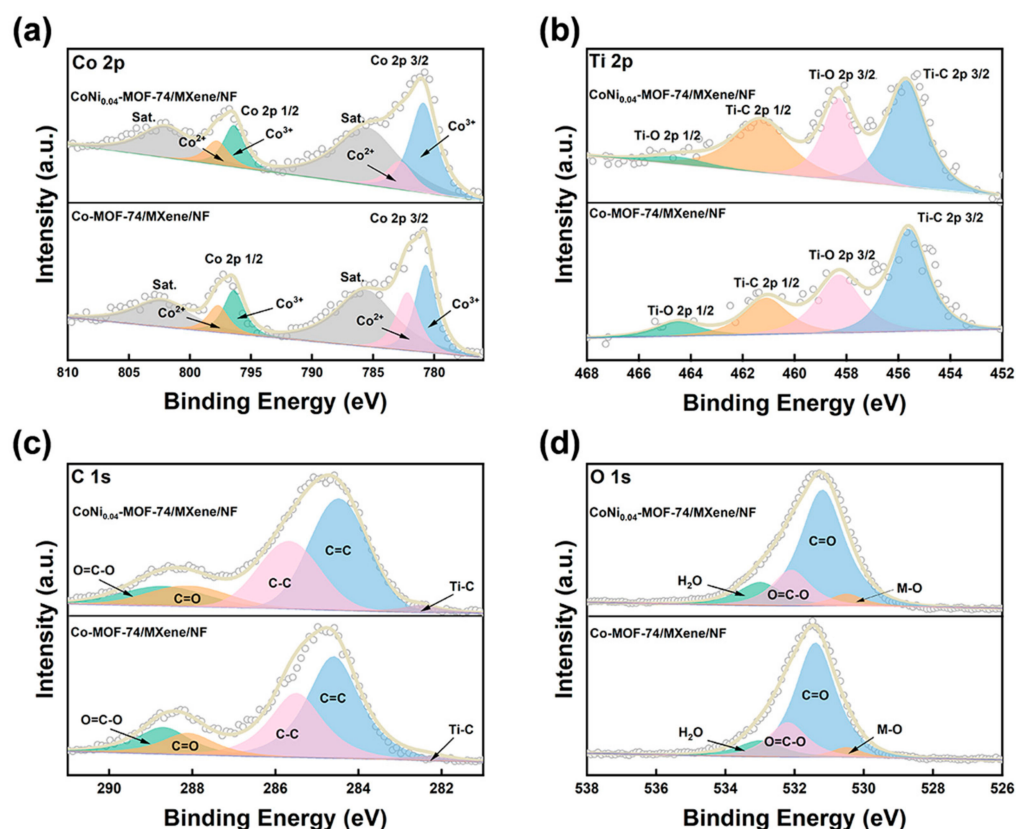


Figure 4. XPS (a) Co 2p, (b) Ti 2p, (c) C 1s, and (d) O 1s spectra of the $\text{CoNi}_{0.04}\text{-MOF/MXene/NF}$ and $\text{Co-MOF-74/MXene/NF}$.

2.2. Oxygen Evolution Reaction Performance

OER typically occurs via a four-electron process on the anode, but it is a slow process with low energy conversion efficiency, while the energy barrier peak represents a major hurdle for electrocatalytic water splitting [35]. The slow reaction kinetics of OER involve

the four-electron process of O=O bond formation. Low overpotential, high current density, and a low Tafel slope value constitute the primary criteria for indicating OER activity [36].

To assess the OER activity, we utilized CoNi_{0.04}-MOF-74/MXene/NF as a self-supporting electrocatalytic electrode for OER in a standard three-electrode system, using 1.0 M KOH. Co-MOF-74/MXene/NF, CoNi_{0.04}-MOF-74/NF and MXene/NF are used as control samples. The polarization curves (Figure 5a) were obtained by performing a linear sweep voltammetry (LSV) test at a sweep rate of 2 mV s⁻¹ with 95% IR compensation. As shown in Figure 5a, the CoNi_{0.04}-MOF-74/MXene/NF composite demonstrates impressive OER activity, achieving an overpotential of 256 mV to deliver a current density of 100 mA/cm². This performance significantly outperforms that of Co-MOF-74/MXene/NF, CoNi_{0.04}-MOF-74/NF, and MXene/NF (Figure 5b), positioning it among the top OER catalysts reported (Table S2, Supplementary Materials), such as Co₂Ni-MOF@MX-1 (η_{10} = 265 mV) [37], Ti₂NT_x@MOF-CoP (η_{50} = 241 mV) [38], MX@MOF-Co₂P (η_{10} = 246 mV) [39], Ti₃C₂@mNiCoP (η_{10} = 237 mV) [40], Ni_{0.7}Fe_{0.3}PS₃@MXene (η_{10} = 283 mV) [41], Mo-NiCoP@MXene/NF (η_{10} = 280 mV) [42], Ru@NiCo-MOF HPNs (η_{10} = 284 mV) [43] and CoNi MOF-CNTs (η_{10} = 306 mV) [44]. Moreover, the intrinsic active sites were evaluated through turn-over frequency (TOF). CoNi_{0.04}-MOF-74/MXene/NF achieves an enhanced TOF of 0.009 s⁻¹ at an overpotential of 200 mV, as shown in Figure S8 (Supplementary Materials). This is significantly higher than those of Co-MOF-74/MXene/NF (0.0042 s⁻¹) and CoNi_{0.04}-MOF-74/NF (0.003 s⁻¹).

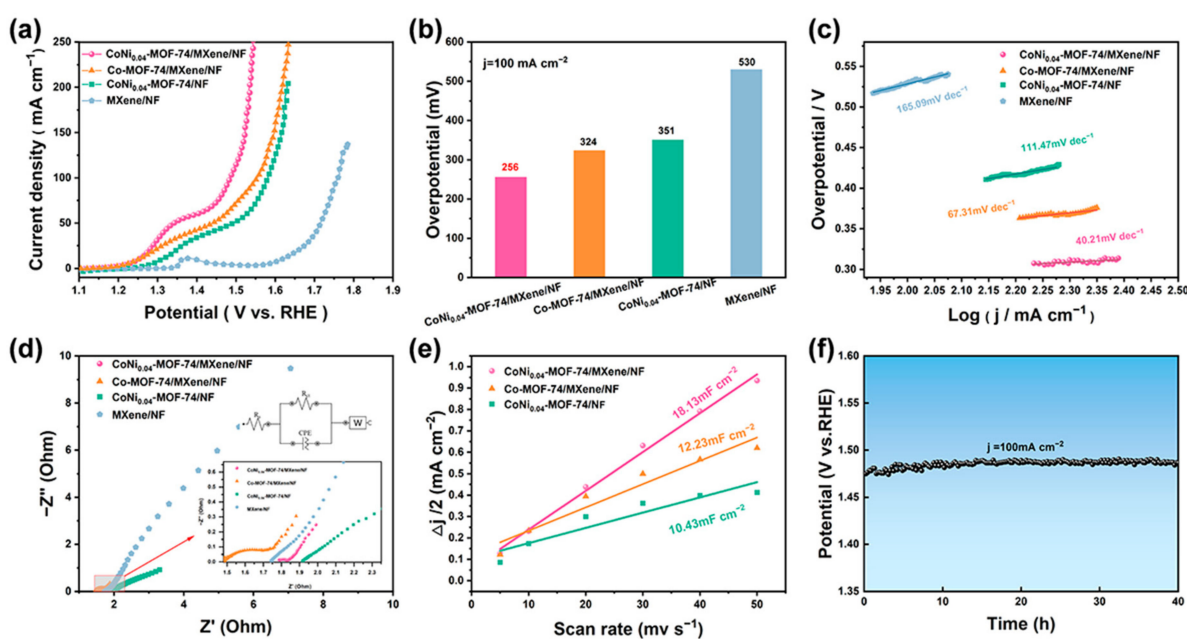


Figure 5. (a) OER polarization curves, (b) overpotential at $j = 100 \text{ mA/cm}^2$, (c) corresponding Tafel plots of various electrodes modified by CoNi_{0.04}-MOF-74/MXene/NF, Co-MOF-74/MXene/NF, CoNi_{0.04}-MOF-74/NF and MXene/NF in 1 M KOH with a scan rate of 2 mV s^{-1} , (d) Nyquist plots, (e) C_{dl} extracted from CV curves of the OER at 1 M KOH, (f) chronopotential of CoNi_{0.04}-MOF-74/MXene/NF at constant anodic current density of 100 mA cm^{-2} .

Given that Ni doping content may influence catalytic performance, the Co/Ni feeding ratio for the catalyst synthesis was optimized. As shown in Figure S9 (Supplementary Materials), among the three catalysts fabricated with various Co/Ni ratios, the CoNi_{0.04}-MOF-74/MXene exhibits the best OER activity with the smallest overpotential and R_{ct} . Therefore, unless otherwise specified, the CoNi_{0.04}-MOF-74/MXene was used for the following work.

To reveal the kinetic behaviors of the catalysts, the smallest Tafel slope of 40.21 mV/dec is achieved by a CoNi_{0.04}-MOF-74/MXene heterostructure compared with those of Co-MOF-74/MXene (67.31 mV/dec), CoNi_{0.04}-MOF-74/NF (111.47 mV/dec) and MXene (165.09 mV/dec), implying the fastest kinetics (Figure 5c). Furthermore, electrochemical

impedance spectroscopy (EIS) was utilized to study the kinetics at the electrode/electrolyte interface of the prepared catalysts. Generally, the electrocatalytic kinetics are influenced by the charge transfer resistance (R_{ct}), with a lower R_{ct} value indicating faster electronic transport. As shown in Figure 5d, the $\text{CoNi}_{0.04}\text{-MOF-74/MXene}$ heterostructure displays a smaller R_{ct} compared to Co-MOF-74/MXene , $\text{CoNi}_{0.04}\text{-MOF-74/NF}$ and MXene (Table S3, Supplementary Materials), which correlates well with the Tafel slope results. R_{ct} and R_s denote charge transfer resistance and equivalent series resistance, respectively; W means Warburg impedance, and CPE is a constant phase element, which simulates the double-layer capacitance. The electrochemically active surface areas (ECSAs) were estimated using the electrochemical double-layer capacitance (C_{dl}) of the catalysts recorded in the non-Faradaic region (0.644–0.744 V vs. RHE). This method was chosen due to its linear relationship with ECSA in 1.0 M KOH (Figure S10, Supplementary Materials). Based on Figure 5e, the C_{dl} value of $\text{CoNi}_{0.04}\text{-MOF-74/MXene}$ (18.13 mF cm^{-2}) is higher than the values for Co-MOF-74/MXene (13.73 mF cm^{-2}) and $\text{CoNi}_{0.04}\text{-MOF-74/NF}$ (10.43 mF cm^{-2}). $\text{CoNi}_{0.04}\text{-MOF-74/MXene}$ displays a greater C_{dl} value, indicating a larger electrochemically active surface area and an increased exposure of active sites. These results demonstrate that the hybridization of MOF-74 with $\text{Ti}_3\text{C}_2\text{T}_x$ MXene can enhance active site exposure, intrinsic activity, and charge transfer kinetics [45].

Stability is another important factor in the assessment of the commercial value of catalysts. The long-term durability of $\text{CoNi}_{0.04}\text{-MOF-74/MXene}$ was measured using chronopotentiometry at $j = 100 \text{ mA/cm}^2$. Even after 40 h of testing, the potential required only increases by 2%, indicating that $\text{CoNi}_{0.04}\text{-MOF-74/MXene}$ has good stability (Figure 5f). Furthermore, there is almost no discernible change in the LSV curve following 1000 cycles of cyclic voltammetry (Figure S11, Supplementary Materials). And the $\text{CoNi}_{0.04}\text{-MOF-74/MXene}$ electrode also maintains relatively intact structural characteristics after 1000 CV cycles. SEM observation confirms the remained micro-rod structure with some nanoflakes on the surface, suggesting good structural stability of the catalyst (Figure S12, Supplementary Materials). TEM characterization further confirms the retention of the micro-rod structure of $\text{CoNi}_{0.04}\text{-MOF-74/MXene}$ after OER and the presence of nanosheets on the surface (Figure S13a, Supplementary Materials). The lattice fringes observed in Figure S13b (Supplementary Materials), measuring 0.233 nm, 0.142 nm, and 0.154 nm, correspond to the (002) plane of Co(OH)_2 (PDF#30-0443) and CoOOH (PDF#26-0480), as well as the (003) crystal plane of Ni(OH)_2 (PDF#14-0117). In addition, selected area electron diffraction detects (101) crystal planes of Co(OH)_2 , and (002) and (131) crystal planes of CoOOH (Figure S13c, Supplementary Materials).

Moreover, the surface chemical composition of the post-OER catalyst was also analyzed using XPS characterization (Figure S14, Supplementary Materials). It is evident that the $\text{Co}^{3+}/\text{Co}^{2+}$ ratio increases from 2.47 to 3.62, and the $\text{Ni}^{3+}/\text{Ni}^{2+}$ ratio increases from 0.34 to 0.54 after OER test (Table S4, Supplementary Materials). This signifies that more reactive hydroxyl oxide substances were generated after OER, as supported by the TEM results. In addition, the increase in M-O content in the O 1s spectrum (Figure S14c, Supplementary Materials) is also corroborated by the production of hydroxyl oxides. In previous reports, Co(Ni)OOH has been identified as the true active species of OER [46–48]. The formed Ni^{3+} and Co^{3+} on the surface possess more valence 3D electron orbitals, leading to higher electron affinity which enhances the adsorption of OER intermediates [46]. Or, following the lattice oxygen mechanism, the formed Co(Ni)OO^- on the catalyst surface may facilitate the evolution of oxygen molecule, boosting the intrinsic catalytic activity for OER [49,50]. In the Ti 2p spectrum (Figure S14d, Supplementary Materials), the disappearance of the Ti-C bond and the increased presence of Ti-O species are attributed to the oxidation of MXene through a prolonged hydrolysis process.

2.3. Hydrogen Evolution Reaction Performance

To achieve high catalyst efficiency for HER in alkaline conditions, two crucial factors must be addressed. One is to improve conductivity. Another crucial aspect is the optimization of the ΔE_{H_2O} and ΔG_H for water and hydrogen adsorption, respectively [51,52].

The HER performance of the as-synthesized catalysts was tested in an alkaline electrolytic cell with a 1 M KOH solution using a three-electrode system. All potentials were converted relative to the reversible hydrogen electrode (RHE) and 95% IR compensation was carried out. In Figure 6a, it can be observed that CoNi_{0.04}-MOF-74/MXene exhibits superior HER activity with a low η_{10} of only 102 mV, which is significantly lower than Co-MOF-74/MXene (175 mV), CoNi_{0.04}-MOF-74/NF (203 mV) and MXene/NF (217 mV) (Figure 6b). The Tafel slope shown in Figure 6c is a significant index for the kinetics of the HER reaction. It is important to note that the mechanisms behind the OER and the HER reactions differ significantly. For the HER in basic media, three primary routes have been proposed, which are as follows:

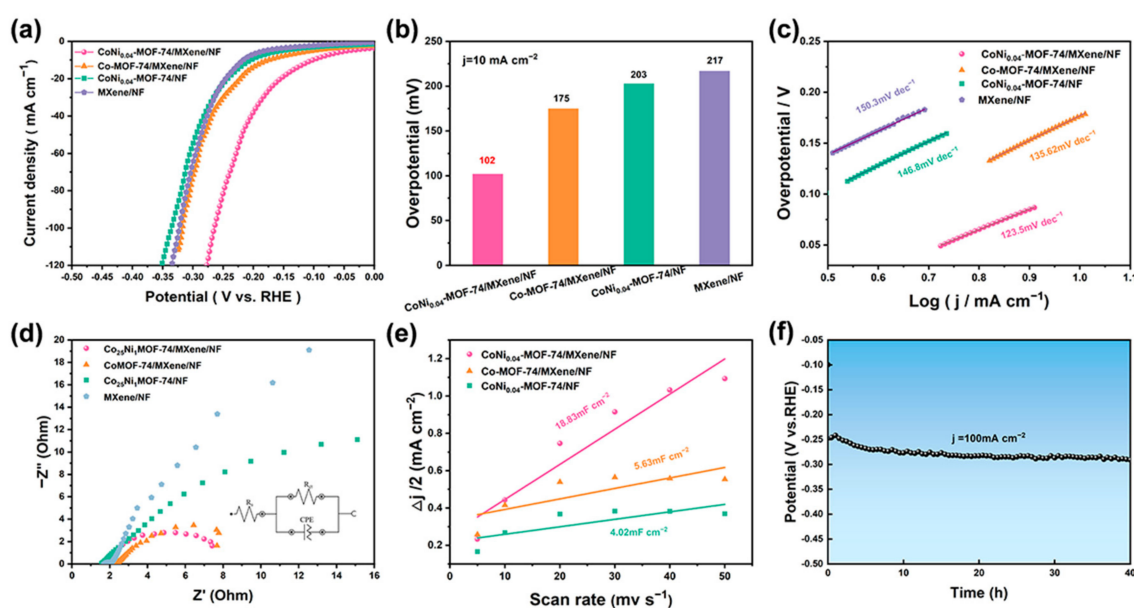
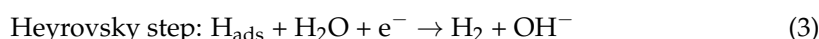
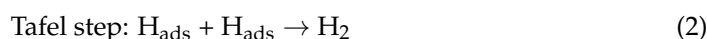
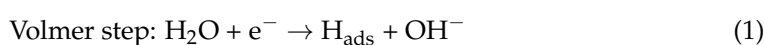


Figure 6. (a) HER polarization curves, (b) overpotential at $j = 10 \text{ mA/cm}^2$, (c) corresponding Tafel plots of various electrodes modified by CoNi_{0.04}-MOF-74/MXene/NF, Co-MOF-74/MXene/NF, CoNi_{0.04}-MOF-74/NF and MXene/NF in 1 M KOH with a scan rate of 5 mV s^{-1} , (d) Nyquist plots, (e) C_{dl} extracted from CV curves of the OER at 1 M KOH, (f) chronopotential of CoNi_{0.04}-MOF-74/MXene/NF at constant anodic current density of 100 mA cm^{-2} .

The reaction routes have a close connection to the Tafel slope. The Tafel slope ranges from approximately 30 to 40 mV dec^{-1} when the rate-determining step (RDS) for HER is either the Heyrovsky or the Tafel step. If the Tafel slope is changed to $\sim 120 \text{ mV dec}^{-1}$, then the RDS becomes the Volmer step [53]. Herein, the Tafel slope of CoNi_{0.04}-MOF-74/MXene ($123.5 \text{ mV dec}^{-1}$) is significantly lower than that of Co-MOF-74/MXene ($135.62 \text{ mV dec}^{-1}$), CoNi_{0.04}-MOF-74/NF ($146.8 \text{ mV dec}^{-1}$) and MXene/NF ($150.3 \text{ mV dec}^{-1}$), indicating faster HER kinetics. Also, the Tafel slope value suggests that the Volmer step is the RDS for our catalysts. The great HER performance of CoNi_{0.04}-MOF-74/MXene was bolstered by the synergistic collaboration of CoNi_{0.04}-MOF-74 and MXene. In particular, MXene speeds up

the Volmer step in HER through augmented catalyst interfacial water adsorption/activation and charged chemical synergistic interactions with MOF. The fantastic hydrophilicity and conductivity of MXene facilitate such interactions, which ultimately affect its HER performance [54,55].

The Nyquist curves display a semicircular shape, which indicates complete control of their electrode reaction processes through the charge transfer process (Figure 6d). In Figure 6d, the R_{ct} of CoNi_{0.04}-MOF-74/MXene is lower compared to Co-MOF-74/MXene, CoNi_{0.04}-MOF-74/NF and MXene/NF, suggesting an accelerated charge transfer process for CoNi_{0.04}-MOF-74/MXene (Table S5, Supplementary Materials). This finding is consistent with the Tafel analysis. Then, the double layer capacitance (C_{dl}) was measured by conducting CV scans at various scanning speeds within a narrow range of the nonfaradic region (0.1–0.2 V) (Figure S15, Supplementary Materials). Figure 6e shows that the CoNi_{0.04}-MOF-74/MXene displays the highest C_{dl} , suggesting that the hybridization of CoNi_{0.04}-MOF-74 with MXene can enhance the ECSA of the material and offer a greater HER reaction site. In addition, the study also measured the average activity of the intrinsically active sites using the turn-over frequency (TOF). As shown in Figure S16 (Supplementary Materials), the TOF of CoNi_{0.04}-MOF-74/MXene is 0.00224 s^{-1} at an overpotential of 100 mV, better than Co-MOF-74/MXene (0.00212 s^{-1}) and CoNi_{0.04}-MOF-74/NF (0.00076 s^{-1}), suggesting the Ni doping enhances the intrinsic activity for HER. The durability of CoNi_{0.04}-MOF-74/MXene was tested using a chronopotentiometer at the current density of 100 mA/cm^2 . Clearly, CoNi_{0.04}-MOF-74/MXene exhibits reasonable stability, with around a 7% increase in the potential even after 40 h of testing (Figure 6f). Furthermore, the LSV curve does not undergo significant changes after 1000 CV cycles (Figure S17, Supplementary Materials). The micro-rod structure of the CoNi_{0.04}-MOF-74/MXene electrodes remains well-preserved even after the HER test (Figure S18, Supplementary Materials). The Raman analysis conducted on post-HER catalyst exhibits peaks at approximately 485 and 503 cm^{-1} , indicating the production of hydroxide and hydroxyl oxide [56–58].

2.4. Overall Water Splitting Performance

Encouraged by the excellent performance of OER and HER, we used CoNi_{0.04}-MOF-74/MXene as both the anode and cathode in a two-electrode system cell to evaluate its ability as a catalyst for overall water splitting. Figure 7a depicts a schematic diagram of the assembly for the alkaline electrolyzer. The results indicate that CoNi_{0.04}-MOF-74/MXene requires only 1.49 V to achieve a current density of 10 mA cm^{-2} , which is significantly better than Pt/C-IrO₂ pair (1.69 V) (Figure 7b). This performance is superior to or comparable to other electrocatalysts reported in the literature (Table S6, Supplementary Materials), such as Ti₂NT_x@MOF-CoP (1.61 V) [38], CdFe-BDC (1.64 V) [59], CoNiBDC/CC (1.625 V) [60], Ni-ZIF/Ni-B@NF (1.54 V) [61], Fe₂Ni-MIL-88B/NFF (1.56 V) [62], NiFe-MOF-74 (1.58 V) [63], NiFe-MOF (1.57 V) [64] and FeMn₆Ce_{0.5}-MOF-74/NF (1.65 V) [65]. Figure 7c shows that the CoNi_{0.04}-MOF-74/MXene electrode maintains a consistent current density of approximately 10 mA cm^{-2} at 1.49 V during a continuous 40 h test. While the Pt/C-IrO₂ pair shows a significant decrease in current density after operation for 40 h. This excellent stability may be attributed to the synergistic effect of MXene and CoNi-MOF-74. The results indicate that the CoNi_{0.04}-MOF-74/MXene material has potential applications as a versatile and efficient electrocatalyst for both the OER and the HER.

The practical application ability of CoNi_{0.04}-MOF-74/MXene in water electrolysis electrochemical systems was evaluated by exploring its electron utilization efficiency. The Faraday efficiency (FE) was measured in 1.0 M KOH. Figure 7d shows that the amount of collected H₂ is approximately double that of collected O₂, consistent with the theoretical ratio of H₂ and O₂ being close to 2:1. This suggests that water has been fully decomposed into oxygen and hydrogen. Upon comparison of the actual molar amount of gas with the theoretical value, the Faraday efficiency was found to be approximately 97.0%. This Faraday efficiency close to 100% indicates that the CoNi_{0.04}-MOF-74/MXene catalyst has great potential as an advanced bifunctional catalyst for electrochemical hydrogen production.

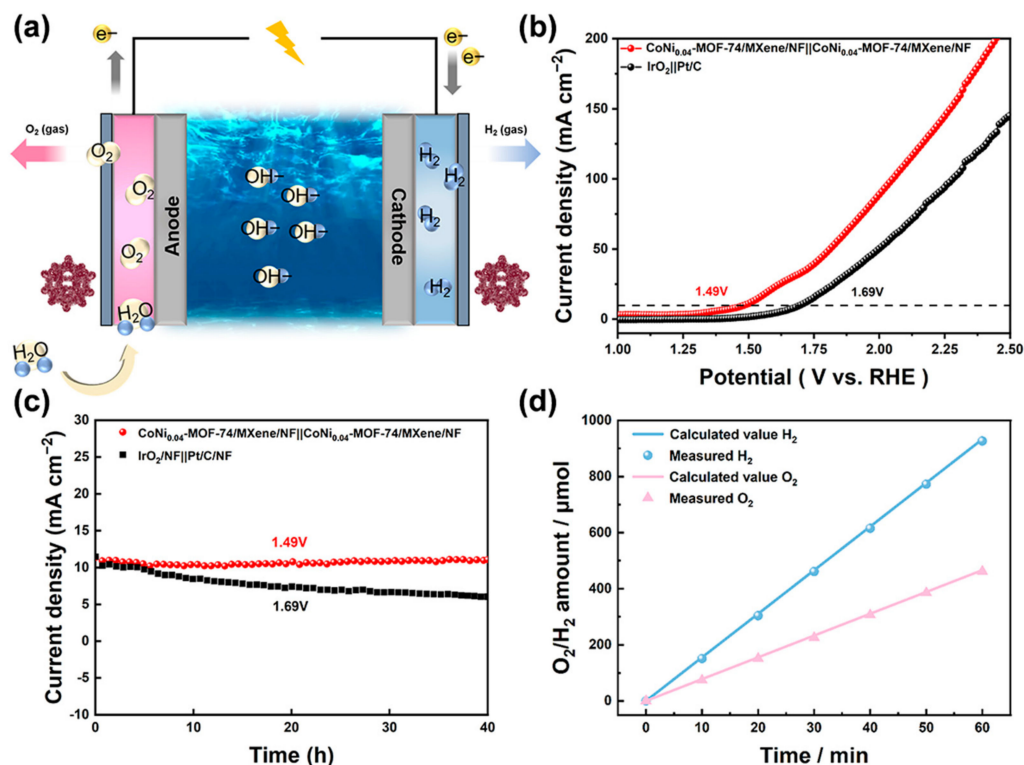


Figure 7. (a) Schematic illustration for the overall water splitting with the CoNi_{0.04}-MOF/MXene/NF couple. (b) The overall water splitting performance of the CoNi_{0.04}-MOF/MXene/NF and Pt/C-IrO₂ couple. (c) The catalytic stability of the CoNi_{0.04}-MOF/MXene/NF and Pt/C-IrO₂ couple for overall water splitting in 1.0 M KOH. (d) Under a current of 50 mA, the calculated and measured H₂ and O₂ production vs. time.

3. Experimental Section

3.1. Materials and Chemicals

Ti₃AlC₂ MAX, Nickel (II) nitrate hexahydrate (Ni(NO₃)₂·6H₂O), cobalt(II) nitrate hexahydrate (Co(NO₃)₂·6H₂O), 2,5-dihydroxyterephthalic acid (H₄DOBDC), N, N-dimethylformamide (DMF) and potassium hydroxide were purchased from Adamas Reagent Co., Ltd. Nickel foam (thickness: 1.6 mm) was obtained from CeTech Co., Ltd (Taichung City, Taiwan). Commercial Pt/C catalyst (20 wt%) were bought from Johnson Matthey Company (Shanghai, China). IrO₂ and nafion (5 wt%) were obtained from Afar Aesar (Shanghai, China). All chemicals were used without further purification.

3.2. Sample Synthesis

3.2.1. Synthesis and Delamination of Ti₃C₂T_x MXene

Ti₃C₂T_x MXene was prepared through the selective etching of the Al layer method using Ti₃AlC₂ powder as the substrate. Firstly, LiF (1.98 g) was added to 20 mL of concentrated HCl and stirred. Then, Ti₃AlC₂ (2 g) powder was slowly added into the above solution and stirred at room temperature for 24 h. The obtained suspension was washed with deionized water and centrifuged several times until the pH of the supernatant reached 6–7. Subsequently, the multilayers of Ti₃C₂T_x were converted into nanosheets by stripping in an ultrasonic machine. Finally, the collected supernatant was dispersed in water to form the desired solution (4 mg·mL⁻¹).

3.2.2. Synthesis of MXene/NF

First, the NF (2 × 3 cm²) was immersed in HCl solution (3 M) for 2 h to remove impurities and oxides, followed by ultrasonic cleaning with acetone, ethanol, and deionized water for 15 min each and drying at 60 °C in an oven. A piece of treated NF (2 × 3 cm²)

was immersed in $\text{Ti}_3\text{C}_2\text{T}_x$ MXene (4 mg mL^{-1}) solution for 1 h and dried in vacuum for 12 h, resulting in the MXene/NF.

3.2.3. Synthesis of $\text{CoNi}_{0.04}$ -MOF-74/MXene/NF

Typically, 2.4 mmol $\text{Co}(\text{NO})_3 \cdot 6\text{H}_2\text{O}$, 0.1 mmol $\text{Ni}(\text{NO})_3 \cdot 6\text{H}_2\text{O}$, and 0.171 g of 2,5-dihydroxybenzene dicarboxylic acid (H_4DOBDC) were dissolved in a mixed solution comprising 10 mL of distilled water, 10 mL of ethanol, and 10 mL of N, N-dimethylformamide (DMF). Subsequently, the resulting solution was transferred to a 50 mL autoclave and the MXene/NF (NF, $2 \times 3 \text{ cm}^2$) prepared above was added and kept at $120 \text{ }^\circ\text{C}$ for 24 h. After cooling to room temperature, the sample was washed with water and ethanol several times, and dried in an oven at $60 \text{ }^\circ\text{C}$. The sample of $\text{CoNi}_{0.04}$ -MOF-74/MXene/NF with a deep-red color on the surface was obtained. For comparison, various catalysts were obtained by maintaining a constant total salt amount of 2.5 mmol and adjusting Co:Ni ratios to be 10:1 or 30:1. Co-MOF-74/MXene/NF catalysts were prepared through the described synthesis without the addition of $\text{Ni}(\text{NO})_3 \cdot 6\text{H}_2\text{O}$.

3.2.4. Synthesis of $\text{CoNi}_{0.04}$ -MOF-74/NF

The $\text{CoNi}_{0.04}$ -MOF-74/NF can be obtained by adding cleaned NF, following the same steps as previously described for synthesis.

3.2.5. Synthesis of Pt/C @NF or IrO_2 @NF

A total of 4 mg of IrO_2 or Pt/C powder samples were dispersed in a mixture of 50 μL of 5 wt% Nafion solution and 950 μL of anhydrous ethanol. The resulting solution was sonicated for 1 h. Subsequently, the prepared solutions were uniformly added to a clean NF, 50 μL at a time, 20 times. The NF was then dried at room temperature.

3.3. Materials Characterization

The morphologies were characterized with field-emission scanning electron microscopy (FE-SEM, Quanta FEG450, Thermo, Waltham, MA, USA) and transmission electron microscopy (TEM, TECNAI F30, Thermo, Waltham, MA, USA). The elemental composition and distribution were investigated with energy dispersive X-ray spectroscopy (EDX, JEOL-2010, Tokyo, Japan) attached to the FE-SEM. The X-ray diffraction (XRD) spectrum was measured using a Bruker D8-Advance X-ray diffractometer (Bruker, Bremen, Germany) with Cu K α radiation to analyze the crystal structure of the samples. The Raman spectrum of the as-prepared samples was conducted with a LabRAM HR 800 system (Horiba Jobin Yvon, Longjumeau, France) at 532 nm laser. FT-IR spectra were recorded in the range of $4000\text{--}450 \text{ cm}^{-1}$ with a JASCO FT/IR-460 spectrophotometer. X-ray photoelectron spectroscopy (XPS, ESCALAB250Xi, Thermo, Waltham, MA, USA) was carried out to analyze the chemical composition and valence states of the constituent elements in the samples.

3.4. Electrochemical Measurement

All electrochemical tests were performed on the Gamry electrochemical workstation (INTERFACE 1010E, Warminster, PA, USA) with a standard three-electrode system, while using the as-obtained catalysts on NF as the working electrode, Pt sheets as the counter electrode, and an Hg/HgO as the reference electrode. A total of 1 M KOH was employed as the electrolyte solution. For HER, the linear sweep voltammograms (LSVs) were measured in a potential range of -0.576 to 0.024 V vs. RHE at a scan rate of 5 mV s^{-1} , while for OER, the LSVs were obtained from 1.024 to 2.024 V vs. RHE at a scan rate of 2 mV s^{-1} . Electrochemical impedance spectroscopy (EIS) was measured in the frequency range of 0.1 Hz to 100 kHz with a 5 mV AC dither for HER and OER, respectively. Cyclic voltammograms (CVs) were tested at different scan rates, which are employed to estimate the double-layer capacitances (C_{dl}) of the catalysts. Chronopotentiometry curves were obtained with a constant current density at 100 mA cm^{-2} . Overall water splitting performance was evaluated in a two-electrode system by using $\text{CoNi}_{0.04}$ -MOF-74/NF as the catalysts

for HER and OER in 1 M KOH. The polarization curves were recorded at a scan rate of 2 mV s^{-1} . The Faraday efficiency (FE) theoretical precipitation is calculated as follows: $n(\text{O}_2) = Q/nF$ ($Q = it$), where $n(\text{O}_2)$ is the theoretical molar amount of O_2 precipitated, Q is the transferred charge, n is the number of electrons transferred in the OER/HER reaction ($n = 4/2$), F is the Faraday's constant ($F = 96,485 \text{ C/mol}$), i is the value of the electric current applied to the water electrolysis, and t is the time of water electrolysis. In this paper, the drainage method was used to derive the amount of oxygen precipitated at a fixed time point, the current applied was 50 mA, and the reaction time of water electrolysis was 1 h. All potentials reported in this paper were converted from vs. Hg/HgO to vs. RHE by adding a value of $0.098 + 0.059 \times \text{pH}$ and were corrected for ohmic losses.

4. Conclusions

A heterostructure electrocatalyst with Ni-doped Co-MOF-74 grown in situ on $\text{Ti}_3\text{C}_2\text{T}_x$ MXene was synthesized using a facile hydrothermal process. Benefiting from the Ni doping and synergistic effect between CoNi-MOF-74 and $\text{Ti}_3\text{C}_2\text{T}_x$, the obtained CoNi-MOF-74/MXene/NF exhibits an impressive electrocatalytic performance, achieving 100 mA/cm^2 at the overpotential of 256 mV for OER and 10 mA/cm^2 at the overpotential of 102 mV, respectively. When employed as both the cathode and anode catalyst, the assembled electrolyzer may drive the current density of 10 mA/cm^2 at a low cell voltage of 1.49 V, meanwhile maintaining excellent durability over 40 h. This work opens a new avenue for improving the activity of transition metal MOF-based catalysts and elucidates the tunability of the catalytic performance through modulating electronic interactions.

Supplementary Materials: The following supporting information can be downloaded at: <https://www.mdpi.com/article/10.3390/catal14030184/s1>. Figure S1. SEM image of as-prepared few-layer $\text{Ti}_3\text{C}_2\text{T}_x$ MXene; Figure S2. SEM images of (a) CoNi_{0.1}-MOF-74/MXene/NF, (b) CoNi_{0.03}-MOF-74/MXene/NF; Figure S3. The SEM (a) and corresponding EDS spectra (b) of CoNi_{0.04}-MOF-74/MXene; Figure S4. XRD patterns of MXene and Ti_3AlC_2 ; Figure S5. XPS survey spectra of CoNi_{0.04}-MOF-74/MXene/NF; Figure S6. XPS (a) Co 2p, (b) Ti 2p, (c) C 1s, and (d) O 1s spectra of the CoNi_{0.04}-MOF-74/MXene/NF and CoNi_{0.04}-MOF-74/NF; Figure S7. Raman spectra of CoNi_{0.04}-MOF-74/MXene/NF; Figure S8. TOF of the CoNi_{0.04}-MOF-74/MXene/NF, Co-MOF-74/MXene/NF and CoNi_{0.04}-MOF-74/NF for OER; Figure S9. CV curves of the CoNi_{0.04}-MOF-74/MXene/NF (a), Co-MOF-74/MXene/NF (b), CoNi_{0.04}-MOF-74/NF (c) under different scan rates in the region of 0.644–0.744 V vs. RHE for OER process; Figure S10. (a) OER polarization curves and (b) Nyquist plots of CoNi_{0.1}-MOF-74/MXene/NF, CoNi_{0.04}-MOF-74/MXene/NF, CoNi_{0.03}-MOF-74/MXene/NF; Figure S11. OER polarization curves for CoNi_{0.04}-MOF-74/MXene/NF before and after 1000 cycles; Figure S12. SEM images of CoNi_{0.04}-MOF-74/MXene/NF after OER test; Figure S13. TEM images of (a) CoNi_{0.04}-MOF-74/MXene/NF after the OER test; HRTEM image (b) and SAED patterns (c) of CoNi_{0.04}-MOF-74/MXene/NF after the OER test; Figure S14. XPS (a) Co 2p, (b) Ni 2p, (c) O 1s, and (d) Ti 2p spectra of the CoNi_{0.04}-MOF-74/MXene/NF and XPS spectra of CoNi_{0.04}-MOF-74 /MXene/NF after the OER test; Figure S15. CV curves of the CoNi_{0.04}-MOF-74/MXene/NF (a), Co-MOF-74/MXene/NF (b), CoNi_{0.04}-MOF-74/NF (c) under different scan rates in the region of 0.1–0.2 V vs. RHE for HER process; Figure S16. TOF of the CoNi_{0.04}-MOF-74/MXene/NF, Co-MOF-74/MXene/NF and CoNi_{0.04}-MOF-74/NF for HER; Figure S17. HER polarization curves for CoNi_{0.04}-MOF-74/MXene/NF before and after 1000 cycles; Figure S18. SEM images of CoNi_{0.04}-MOF-74/MXene/NF after HER test; Figure S19. Raman spectra of CoNi_{0.04}-MOF-74/MXene/NF after the HER test; Table S1. Co2p peak area ratio of CoNi_{0.04}-MOF-74/MXene/NF and Co-MOF-74/MXene/NF calculated from XPS spectra; Table S2. Comparison of Electrochemical performances of OER of CoNi_{0.04}-MOF-74/MXene/NF with recently reported OER electrocatalysts in 1 M KOH; Table S3. OER catalyst EIS fitting parameters; Table S4. Area ratios in Co2p and Ni2p peaks calculated from XPS spectra for CoNi_{0.04}-MOF-74/MXene/NF and that after OER testing; Table S5. HER catalyst EIS fitting parameters; Table S6. Comparison of Electrochemical performances of OWS of CoNi_{0.04}-MOF-74/MXene/NF with recently reported OWS electrocatalysts in 1 M KOH. References [37–44,59–65] have been cited in the Supplementary Materials.

Author Contributions: K.Y.: Writing—original draft, data curation, methodology, investigation, validation. J.Z.: Data curation, validation. Y.H.: data curation, methodology. L.W.: Methodology. X.Z.: Methodology. B.Z.: Funding acquisition, conceptualization, writing—review and editing. All authors have read and agreed to the published version of the manuscript.

Funding: Financial support from the Natural Science Foundation of Shanghai (21ZR1445700) and the Science and Technology Commission of Shanghai Municipality (23440790402) is gratefully acknowledged.

Data Availability Statement: The article includes all relevant data, as confirmed by the authors.

Conflicts of Interest: The authors declare no competing financial interests or personal relationships that could have appeared to influence the work reported in this paper.

References

1. Li, J.; Hou, C.; Chen, C.; Ma, W.; Li, Q.; Hu, L.; Lv, X.; Dang, J. Collaborative Interface Optimization Strategy Guided Ultrafine RuCo and MXene Heterostructure Electrocatalysts for Efficient Overall Water Splitting. *ACS Nano* **2023**, *17*, 10947–10957. [[CrossRef](#)] [[PubMed](#)]
2. He, Y.; Shen, J.; Li, Q.; Zheng, X.; Wang, Z.; Cui, L.; Xu, J.; Liu, J. In-situ growth of VS₄ nanorods on Ni-Fe sulfides nanoplate array towards achieving a highly efficient and bifunctional electrocatalyst for total water splitting. *Chem. Eng. J.* **2023**, *474*, 145461. [[CrossRef](#)]
3. Abdelghafar, F.; Xu, X.; Jiang, S.P.; Shao, Z. Designing single-atom catalysts toward improved alkaline hydrogen evolution reaction. *Mater. Rep. Energy* **2022**, *2*, 100144. [[CrossRef](#)]
4. Yu, M.; Zheng, J.; Guo, M. La-doped NiFe-LDH coupled with hierarchical vertically aligned MXene frameworks for efficient overall water splitting. *J. Energy Chem.* **2022**, *70*, 472–479. [[CrossRef](#)]
5. Tang, J.; Xu, X.; Tang, T.; Zhong, Y.; Shao, Z. Perovskite-Based Electrocatalysts for Cost-Effective Ultrahigh-Current-Density Water Splitting in Anion Exchange Membrane Electrolyzer Cell. *Small Methods* **2022**, *6*, 2201099. [[CrossRef](#)] [[PubMed](#)]
6. Wu, J.; Yu, Z.; Zhang, Y.; Niu, S.; Zhao, J.; Li, S.; Xu, P. Understanding the Effect of Second Metal on CoM (M = Ni, Cu, Zn) Metal–Organic Frameworks for Electrocatalytic Oxygen Evolution Reaction. *Small* **2021**, *17*, 2105150. [[CrossRef](#)] [[PubMed](#)]
7. Zhou, J.-J.; Ji, W.; Xu, L.; Yang, Y.; Wang, W.; Ding, H.; Xu, X.; Wang, W.; Zhang, P.; Hua, Z.; et al. Controllable transformation of CoNi-MOF-74 on Ni foam into hierarchical-porous Co(OH)₂/Ni(OH)₂ micro-rods with ultra-high specific surface area for energy storage. *Chem. Eng. J.* **2022**, *428*, 132123. [[CrossRef](#)]
8. Zhao, L.; Dong, B.; Li, S.; Zhou, L.; Lai, L.; Wang, Z.; Zhao, S.; Han, M.; Gao, K.; Lu, M.; et al. Interdiffusion Reaction-Assisted Hybridization of Two-Dimensional Metal–Organic Frameworks and Ti₃C₂T_x Nanosheets for Electrocatalytic Oxygen Evolution. *ACS Nano* **2017**, *11*, 5800–5807. [[CrossRef](#)]
9. Lu, X.F.; Fang, Y.; Luan, D.; Lou, X.W.D. Metal–Organic Frameworks Derived Functional Materials for Electrochemical Energy Storage and Conversion: A Mini Review. *Nano Lett.* **2021**, *21*, 1555–1565. [[CrossRef](#)]
10. Xu, X.; Sun, H.; Jiang, S.P.; Shao, Z. Modulating metal–organic frameworks for catalyzing acidic oxygen evolution for proton exchange membrane water electrolysis. *SusMat* **2021**, *1*, 460–481. [[CrossRef](#)]
11. Romero-Muñiz, C.; Gavira-Vallejo, J.M.; Merklings, P.J.; Calero, S. Impact of Small Adsorbates in the Vibrational Spectra of Mg- and Zn-MOF-74 Revealed by First-Principles Calculations. *ACS Appl. Mater. Interfaces* **2020**, *12*, 54980–54990. [[CrossRef](#)]
12. Vornholt, S.M.; Duncan, M.J.; Warrender, S.J.; Semino, R.; Ramsahye, N.A.; Maurin, G.; Smith, M.W.; Tan, J.-C.; Miller, D.N.; Morris, R.E. Multifaceted Study of the Interactions between CPO-27-Ni and Polyurethane and Their Impact on Nitric Oxide Release Performance. *ACS Appl. Mater. Interfaces* **2020**, *12*, 58263–58276. [[CrossRef](#)]
13. Abednatanzi, S.; Derakhshandeh, P.G.; Depauw, H.; Coudert, F.-X.; Vrielinck, H.; Van Der Voort, P.; Leus, K. Mixed-metal metal–organic frameworks. *Chem. Soc. Rev.* **2019**, *48*, 2535–2565. [[CrossRef](#)] [[PubMed](#)]
14. Gutiérrez-Tarriño, S.; Olloqui-Sariego, J.L.; Calvente, J.J.; Palomino, M.; Espallargas, G.M.; Jordá, J.L.; Rey, F.; Oña-Burgos, P. Cobalt Metal–Organic Framework Based on Two Dinuclear Secondary Building Units for Electrocatalytic Oxygen Evolution. *ACS Appl. Mater. Interfaces* **2019**, *11*, 46658–46665. [[CrossRef](#)] [[PubMed](#)]
15. Wu, Y.; Li, Y.; Gao, J.; Zhang, Q. Recent advances in vacancy engineering of metal-organic frameworks and their derivatives for electrocatalysis. *SusMat* **2021**, *1*, 66–87. [[CrossRef](#)]
16. Yan, L.; Cao, L.; Dai, P.; Gu, X.; Liu, D.; Li, L.; Wang, Y.; Zhao, X. Metal-organic Frameworks Derived Nanotube of Nickel–Cobalt Bimetal Phosphides as Highly Efficient Electrocatalysts for Overall Water Splitting. *Adv. Funct. Mater.* **2017**, *27*, 1703455. [[CrossRef](#)]
17. Zhu, Q.-L.; Xu, Q. Metal–organic framework composites. *Chem. Soc. Rev.* **2014**, *43*, 5468–5512. [[CrossRef](#)]
18. Liu, C.; Bai, Y.; Li, W.; Yang, F.; Zhang, G.; Pang, H. In Situ Growth of Three-Dimensional MXene/Metal–Organic Framework Composites for High-Performance Supercapacitors. *Angew. Chem. Int. Ed. Engl.* **2022**, *61*, e202116282. [[CrossRef](#)]
19. Chen, Y.; Yao, H.; Kong, F.; Tian, H.; Meng, G.; Wang, S.; Mao, X.; Cui, X.; Hou, X.; Shi, J. V₂C MXene synergistically coupling FeNi LDH nanosheets for boosting oxygen evolution reaction. *Appl. Catal. B Environ.* **2021**, *297*, 120474. [[CrossRef](#)]
20. Zhang, L.; Wang, Z.; Chen, W.; Yuan, R.; Zhan, K.; Zhu, M.; Yang, J.; Zhao, B. Fe₃O₄ nanoplates anchored on Ti₃C₂T_x MXene with enhanced pseudocapacitive and electrocatalytic properties. *Nanoscale* **2021**, *13*, 15343–15351. [[CrossRef](#)]

21. Yue, X.; Dong, Y.; Cao, H.; Wei, X.; Zheng, Q.; Sun, W.; Lin, D. Effect of electronic structure modulation and layer spacing change of NiAl layered double hydroxide nanoflowers caused by cobalt doping on supercapacitor performance. *J. Colloid Interface Sci.* **2023**, *630*, 973–983. [[CrossRef](#)]
22. Chen, L.; Zhang, Y.; Li, D.; Wang, Y.; Duan, C. Magnesium-regulated oxygen vacancies of nickel layered double hydroxides for electrocatalytic water oxidation. *J. Mater. Chem. A* **2018**, *6*, 18378–18383. [[CrossRef](#)]
23. Feng, X.; Jiao, Q.; Chen, W.; Dang, Y.; Dai, Z.; Suib, S.L.; Zhang, J.; Zhao, Y.; Li, H.; Feng, C. Cactus-like NiCo₂S₄@NiFe LDH hollow spheres as an effective oxygen bifunctional electrocatalyst in alkaline solution. *Appl. Catal. B Environ.* **2021**, *286*, 119869. [[CrossRef](#)]
24. Wu, C.; Zhang, X.; Li, H.; Xia, Z.; Yu, S.; Wang, S.; Sun, G. Iron-based binary metal-organic framework nanorods as an efficient catalyst for the oxygen evolution reaction. *Chin. J. Catal.* **2021**, *42*, 637–647. [[CrossRef](#)]
25. Zhou, J.; Han, Z.; Wang, X.; Gai, H.; Chen, Z.; Guo, T.; Hou, X.; Xu, L.; Hu, X.; Huang, M.; et al. Discovery of Quantitative Electronic Structure-OER Activity Relationship in Metal-Organic Framework Electrocatalysts Using an Integrated Theoretical-Experimental Approach. *Adv. Funct. Mater.* **2021**, *31*, 2102066. [[CrossRef](#)]
26. Wang, S.; Li, Q.; Sun, S.; Ge, K.; Zhao, Y.; Yang, K.; Zhang, Z.; Cao, J.; Lu, J.; Yang, Y.; et al. Heterostructured ferroelectric BaTiO₃@MOF-Fe/Co electrocatalysts for efficient oxygen evolution reaction. *J. Mater. Chem. A* **2022**, *10*, 5350–5360. [[CrossRef](#)]
27. Liu, Z.; Li, H.; Kang, H.-S.; N'Diaye, A.T.; Lee, M.H. Lattice oxygen-mediated NiOOM formation for efficient oxygen evolution reaction in MOF@LDH core-shell structures. *Chem. Eng. J.* **2023**, *454*, 140403. [[CrossRef](#)]
28. Papadakis, G.; Tsortos, A.; Kordas, A.; Tiniakou, I.; Morou, E.; Vontas, J.; Kardassis, D.; Gizeli, E. Acoustic detection of DNA conformation in genetic assays combined with PCR. *Sci. Rep.* **2013**, *3*, 2033. [[CrossRef](#)] [[PubMed](#)]
29. Wang, L.; Song, L.; Yang, Z.; Chang, Y.-M.; Hu, F.; Li, L.; Li, L.; Chen, H.-Y.; Peng, S. Electronic Modulation of Metal-Organic Frameworks by Interfacial Bridging for Efficient pH-Universal Hydrogen Evolution. *Adv. Funct. Mater.* **2023**, *33*, 2210322. [[CrossRef](#)]
30. Karlsson, L.H.; Birch, J.; Halim, J.; Barsoum, M.W.; Persson, P.O.Å. Atomically Resolved Structural and Chemical Investigation of Single MXene Sheets. *Nano Lett.* **2015**, *15*, 4955–4960. [[CrossRef](#)]
31. Yang, D.; Velamakanni, A.; Bozoklu, G.; Park, S.; Stoller, M.; Piner, R.D.; Stankovich, S.; Jung, I.; Field, D.A.; Ventrice, C.A.; et al. Chemical analysis of graphene oxide films after heat and chemical treatments by X-ray photoelectron and Micro-Raman spectroscopy. *Carbon* **2009**, *47*, 145–152. [[CrossRef](#)]
32. Jiang, W.; Wang, J.; Jiang, Y.; Wu, Y.; Liu, B.; Chu, X.; Liu, C.; Che, G.; Lu, Y. Multivalent ruthenium immobilized by self-supported NiFe-organic frameworks for efficient electrocatalytic overall water splitting. *J. Mater. Chem. A* **2023**, *11*, 2769–2779. [[CrossRef](#)]
33. Strauss, I.; Mundstock, A.; Hinrichs, D.; Himstedt, R.; Knebel, A.; Reinhardt, C.; Dorfs, D.; Caro, J. The Interaction of Guest Molecules with Co-MOF-74: A Vis/NIR and Raman Approach. *Angew. Chem. Int. Ed.* **2018**, *57*, 7434–7439. [[CrossRef](#)] [[PubMed](#)]
34. Wu, T.; Shi, Y.; Wang, Z.; Liu, C.; Bi, J.; Yu, Y.; Wu, L. Unsaturated NiII Centers Mediated the Coordination Activation of Benzylamine for Enhancing Photocatalytic Activity over Ultrathin Ni MOF-74 Nanosheets. *ACS Appl. Mater. Interfaces* **2021**, *13*, 61286–61295. [[CrossRef](#)]
35. Zhang, Y.-C.; Han, C.; Gao, J.; Pan, L.; Wu, J.; Zhu, X.-D.; Zou, J.-J. NiCo-Based Electrocatalysts for the Alkaline Oxygen Evolution Reaction: A Review. *ACS Catal.* **2021**, *11*, 12485–12509. [[CrossRef](#)]
36. Shi, J.; Qiu, F.; Yuan, W.; Guo, M.; Lu, Z.-H. Nitrogen-doped carbon-decorated yolk-shell CoP@FeCoP micro-polyhedra derived from MOF for efficient overall water splitting. *Chem. Eng. J.* **2021**, *403*, 126312. [[CrossRef](#)]
37. Tan, P.; Gao, R.; Zhang, Y.; Han, N.; Jiang, Y.; Xu, M.; Bao, S.-J.; Zhang, X. Electrostatically directed assembly of two-dimensional ultrathin Co₂Ni-MOF/Ti₃C₂T_x nanosheets for electrocatalytic oxygen evolution. *J. Colloid Interface Sci.* **2023**, *630*, 363–371. [[CrossRef](#)] [[PubMed](#)]
38. Zong, H.; Qi, R.; Yu, K.; Zhu, Z. Ultrathin Ti₂NT_x MXene-wrapped MOF-derived CoP frameworks towards hydrogen evolution and water oxidation. *Electrochim. Acta* **2021**, *393*, 139068. [[CrossRef](#)]
39. Li, J.; Chen, C.; Lv, Z.; Ma, W.; Wang, M.; Li, Q.; Dang, J. Constructing heterostructures of ZIF-67 derived C, N doped Co₂P and Ti₂VC₂T_x MXene for enhanced OER. *J. Mater. Sci. Technol.* **2023**, *145*, 74–82. [[CrossRef](#)]
40. Yue, Q.; Sun, J.; Chen, S.; Zhou, Y.; Li, H.; Chen, Y.; Zhang, R.; Wei, G.; Kang, Y. Hierarchical Mesoporous MXene-NiCoP Electrocatalyst for Water-Splitting. *ACS Appl. Mater. Interfaces* **2020**, *12*, 18570–18577. [[CrossRef](#)]
41. Du, C.-F.; Dinh, K.N.; Liang, Q.; Zheng, Y.; Luo, Y.; Zhang, J.; Yan, Q. Self-Assemble and In Situ Formation of Ni_{1-x}Fe_xPS₃ Nanomosaic-Decorated MXene Hybrids for Overall Water Splitting. *Adv. Energy Mater.* **2018**, *8*, 1801127. [[CrossRef](#)]
42. Jiang, J.; Sun, R.; Huang, X.; Xu, W.; Zhou, S.; Wei, Y.; Han, S.; Li, Y. In-situ derived Mo-doped NiCoP and MXene to form Mott-Schottky heterojunction with tunable surface electron density to promote overall water splitting. *Compos. Part B Eng.* **2023**, *263*, 110834. [[CrossRef](#)]
43. Liu, D.; Xu, H.; Wang, C.; Shang, H.; Yu, R.; Wang, Y.; Li, J.; Li, X.; Du, Y. 3D Porous Ru-Doped NiCo-MOF Hollow Nanospheres for Boosting Oxygen Evolution Reaction Electrocatalysis. *Inorg. Chem.* **2021**, *60*, 5882–5889. [[CrossRef](#)] [[PubMed](#)]
44. Yu, S.; Wu, Y.; Xue, Q.; Zhu, J.-J.; Zhou, Y. A novel multi-walled carbon nanotube-coupled CoNi MOF composite enhances the oxygen evolution reaction through synergistic effects. *J. Mater. Chem. A* **2022**, *10*, 4936–4943. [[CrossRef](#)]
45. Hu, L.; Xiao, R.; Wang, X.; Wang, X.; Wang, C.; Wen, J.; Gu, W.; Zhu, C. MXene-induced electronic optimization of metal-organic framework-derived CoFe LDH nanosheet arrays for efficient oxygen evolution. *Appl. Catal. B Environ.* **2021**, *298*, 120599. [[CrossRef](#)]

46. Li, M.; Sun, R.; Li, Y.; Jiang, J.; Xu, W.; Cong, H.; Han, S. The 3D porous “celosia” heterogeneous interface engineering of layered double hydroxide and P-doped molybdenum oxide on MXene promotes overall water-splitting. *Chem. Eng. J.* **2022**, *431*, 133941. [[CrossRef](#)]
47. Han, J.; Zhang, J.; Wang, T.; Xiong, Q.; Wang, W.; Cao, L.; Dong, B. Zn Doped FeCo Layered Double Hydroxide Nanoneedle Arrays with Partial Amorphous Phase for Efficient Oxygen Evolution Reaction. *ACS Sustain. Chem. Eng.* **2019**, *7*, 13105–13114. [[CrossRef](#)]
48. Wang, H.-Y.; Hung, S.-F.; Chen, H.-Y.; Chan, T.-S.; Chen, H.M.; Liu, B. In Operando Identification of Geometrical-Site-Dependent Water Oxidation Activity of Spinel Co₃O₄. *J. Am. Chem. Soc.* **2015**, *138*, 36–39. [[CrossRef](#)] [[PubMed](#)]
49. Wang, X.; Xing, C.; Liang, Z.; Guardia, P.; Han, X.; Zuo, Y.; Llorca, J.; Arbiol, J.; Li, J.; Cabot, A. Activating the lattice oxygen oxidation mechanism in amorphous molybdenum cobalt oxide nanosheets for water oxidation. *J. Mater. Chem. A* **2022**, *10*, 3659–3666. [[CrossRef](#)]
50. Moysiadou, A.; Lee, S.; Hsu, C.-S.; Chen, H.M.; Hu, X. Mechanism of Oxygen Evolution Catalyzed by Cobalt Oxyhydroxide: Cobalt Superoxide Species as a Key Intermediate and Dioxygen Release as a Rate-Determining Step. *J. Am. Chem. Soc.* **2020**, *142*, 11901–11914. [[CrossRef](#)] [[PubMed](#)]
51. Wei, Z.; Zhao, Z.; Wang, J.; Zhou, Q.; Zhao, C.; Yao, Z.; Wang, J. Oxygen-deficient TiO₂ and carbon coupling synergistically boost the activity of Ru nanoparticles for the alkaline hydrogen evolution reaction. *J. Mater. Chem. A* **2021**, *9*, 10160–10168. [[CrossRef](#)]
52. Kuang, P.; Wang, Y.; Zhu, B.; Xia, F.; Tung, C.-W.; Wu, J.; Chen, H.M.; Yu, J. Pt Single Atoms Supported on N-Doped Mesoporous Hollow Carbon Spheres with Enhanced Electrocatalytic H₂-Evolution Activity. *Adv. Mater.* **2021**, *33*, 2008599. [[CrossRef](#)]
53. Lv, J.; Liu, P.; Li, R.; Wang, L.; Zhang, K.; Zhou, P.; Huang, X.; Wang, G. Constructing accelerated charge transfer channels along V-Co-Fe via introduction of V into CoFe-layered double hydroxides for overall water splitting. *Appl. Catal. B Environ.* **2021**, *298*, 120587. [[CrossRef](#)]
54. Yu, M.; Wang, Z.; Liu, J.; Sun, F.; Yang, P.; Qiu, J. A hierarchically porous and hydrophilic 3D nickel-iron/MXene electrode for accelerating oxygen and hydrogen evolution at high current densities. *Nano Energy* **2019**, *63*, 103880. [[CrossRef](#)]
55. Yu, M.; Zhou, S.; Wang, Z.; Zhao, J.; Qiu, J. Boosting electrocatalytic oxygen evolution by synergistically coupling layered double hydroxide with MXene. *Nano Energy* **2018**, *44*, 181–190. [[CrossRef](#)]
56. Li, D.; Xiang, R.; Yu, F.; Zeng, J.; Zhang, Y.; Zhou, W.; Liao, L.; Zhang, Y.; Tang, D.; Zhou, H. In Situ Regulating Cobalt/Iron Oxide-Oxyhydroxide Exchange by Dynamic Iron Incorporation for Robust Oxygen Evolution at Large Current Density. *Adv. Mater.* **2023**, *36*, 2305685. [[CrossRef](#)] [[PubMed](#)]
57. Jia, Z.; Yuan, Y.; Zhang, Y.; Lyu, X.; Liu, C.; Yang, X.; Bai, Z.; Wang, H.; Yang, L. Optimizing 3d spin polarization of CoOOH by in situ Mo doping for efficient oxygen evolution reaction. *Carbon Energy* **2023**, *6*, e418. [[CrossRef](#)]
58. Zhu, Y.; An, S.; Sun, X.; Lan, D.; Cui, J.; Zhang, Y.; He, W. Core-branched NiCo₂S₄@CoNi-LDH heterostructure as advanced electrode with superior energy storage performance. *Chem. Eng. J.* **2020**, *383*, 123206. [[CrossRef](#)]
59. Luo, Y.; Yang, X.; He, L.; Zheng, Y.; Pang, J.; Wang, L.; Jiang, R.; Hou, J.; Guo, X.; Chen, L. Structural and Electronic Modulation of Iron-Based Bimetallic Metal–Organic Framework Bifunctional Electrocatalysts for Efficient Overall Water Splitting in Alkaline and Seawater Environment. *ACS Appl. Mater. Interfaces* **2022**, *14*, 46374–46385. [[CrossRef](#)] [[PubMed](#)]
60. Bai, X.-J.; Chen, H.; Li, Y.-N.; Shao, L.; Ma, J.-C.; Li, L.-L.; Chen, J.-Y.; Wang, T.-Q.; Zhang, X.-M.; Zhang, L.-Y.; et al. CoNi-based metal–organic framework nanoarrays supported on carbon cloth as bifunctional electrocatalysts for efficient water-splitting. *New J. Chem.* **2020**, *44*, 1694–1698. [[CrossRef](#)]
61. Xu, H.; Fei, B.; Cai, G.; Ha, Y.; Liu, J.; Jia, H.; Zhang, J.; Liu, M.; Wu, R. Boronization-Induced Ultrathin 2D Nanosheets with Abundant Crystalline–Amorphous Phase Boundary Supported on Nickel Foam toward Efficient Water Splitting. *Adv. Energy Mater.* **2020**, *10*, 1902714. [[CrossRef](#)]
62. Raja, D.S.; Chuah, X.-F.; Lu, S.-Y. In Situ Grown Bimetallic MOF-Based Composite as Highly Efficient Bifunctional Electrocatalyst for Overall Water Splitting with Ultrastability at High Current Densities. *Adv. Energy Mater.* **2018**, *8*, 1801065. [[CrossRef](#)]
63. Chen, C.; Suo, N.; Han, X.; He, X.; Dou, Z.; Lin, Z.; Cui, L. Tuning the morphology and electron structure of metal-organic framework-74 as bifunctional electrocatalyst for OER and HER using bimetallic collaboration strategy. *J. Alloys Compd.* **2021**, *865*, 158795. [[CrossRef](#)]
64. Mou, Q.; Xu, Z.; Wang, G.; Li, E.; Liu, J.; Zhao, P.; Liu, X.; Li, H.; Cheng, G. A bimetal hierarchical layer structure MOF grown on Ni foam as a bifunctional catalyst for the OER and HER. *Inorg. Chem. Front.* **2021**, *8*, 2889–2899. [[CrossRef](#)]
65. Chai, N.; Kong, Y.; Liu, T.; Ying, S.; Jiang, Q.; Yi, F.-Y. (FeMnCe)-co-doped MOF-74 with significantly improved performance for overall water splitting. *Dalton Trans.* **2023**, *52*, 11601–11610. [[CrossRef](#)] [[PubMed](#)]

Disclaimer/Publisher’s Note: The statements, opinions and data contained in all publications are solely those of the individual author(s) and contributor(s) and not of MDPI and/or the editor(s). MDPI and/or the editor(s) disclaim responsibility for any injury to people or property resulting from any ideas, methods, instructions or products referred to in the content.